Journal of Materials Chemistry A

ROYAL SOCIETY OF CHEMISTRY

PAPER

View Article Online
View Journal | View Issue

Cite this: J. Mater. Chem. A, 2025, 13, 39970

Breaking barriers in nitrate electroreduction: robust Cu–Zn catalysts for selective ammonia production with ultra-high rate in neutral medium

Abdelrahman M. Abdelmohsen, [a] Lobna A. Abdo,[a] Ghada E. Khedr [b] and Nageh K. Allam *[a]

The electrocatalytic nitrate reduction reaction (NO_3^-RR) offers a sustainable route for ammonia synthesis under ambient conditions, presenting a more environmentally favorable alternative to the energy-intensive Haber–Bosch process. Achieving this transformation through emission-free fabrication methods positions NO_3^-RR as a highly attractive target for advanced research. However, realizing efficient NO_3^-RR remains challenging due to persistent issues with operational stability, selectivity, efficiency, and long-term performance, particularly in neutral media. In this study, we developed a robust, engineered Cu–Zn alloy catalyst system, with the $Cu_{85}Zn_{15}$ composition exhibiting the highest activity among all tested variants. In a neutral electrolyte, $Cu_{85}Zn_{15}$ achieved an exceptional faradaic efficiency of approximately 98% and an impressive ammonia yield rate of 2.8 mmol h^{-1} cm^{-2} at −0.8 V *vs.* RHE, surpassing most reported copper-based catalysts. The catalyst demonstrated remarkable durability, maintaining high selectivity and activity over 10 consecutive electrochemical cycles and sustaining continuous operation for over 170 hours, underscoring its potential for industrial application. Comprehensive surface characterization, including atomic force microscopy (AFM), electrochemical surface area (ECSA) analysis, underpotential deposition of lead (UPD-Pb), and electrochemical impedance spectroscopy (EIS), revealed that Zn incorporation enhanced surface roughness and created additional active sites. Notably, these enhancements were optimized at a Zn content of 15%; other compositions exhibited only moderate performance improvements. DFT calculations revealed that the $Cu_{85}Zn_{15}$ alloy optimally balances NO_3^- adsorption and intermediate stabilization, enabling low energy barriers for key steps in ammonia formation. Its unique Cu–Zn active sites enhance NO_3^- activation and suppress competing hydrogen evolution, explaining its superior NO_3RR performance. Overall, this work highlights the high operational efficiency of Cu–Zn alloys under neutral conditions and demonstrates their promise for scalable industrial applications, owing to their low cost, long-term stability, and the natural abundance of constituent elements.

Received 18th September 2025
Accepted 20th October 2025

DOI: 10.1039/d5ta07667f

rsc.li/materials-a

Introduction

Ammonia (NH_3) plays a critical role in global agriculture, industrial synthesis, and increasingly, energy storage and conversion technologies due to its high hydrogen content and ease of liquefaction.[1,2] Despite its centrality in modern infrastructure, the conventional Haber–Bosch process used for ammonia synthesis is highly energy-intensive, operating under harsh thermodynamic conditions (400–500 °C and 150–300 atm) and accounting for nearly 2% of global energy consumption and approximately 1% of global CO_2 emissions.[3–5] This reliance on fossil-derived hydrogen and extreme operating conditions has catalyzed interest in developing alternative, sustainable methods for NH_3 production.

Electrochemical approaches, particularly the nitrogen reduction reaction (NRR), have garnered attention for their potential to generate NH_3 under ambient conditions using renewable electricity.[6–8] However, NRR faces inherent limitations stemming from the low aqueous solubility of nitrogen (0.66 mmol L^{-1}) and the formidable bond energy of the N≡N triple bond (945 kJ mol^{-1}), which severely hinders reaction kinetics and selectivity.[9,10] These challenges have shifted focus toward the electrochemical nitrate reduction reaction (NO_3RR), which offers a thermodynamically favorable pathway to ammonia owing to the lower dissociation energies of the N–O (176 kJ mol^{-1}) and N=O (204 kJ mol^{-1}) bonds in nitrate species.[10–13] Nitrate contamination is a widespread environmental issue resulting from the overuse of nitrogen-rich

[a]Energy Materials Laboratory, Physics Department, School of Sciences and Engineering, The American University in Cairo, New Cairo 11835, Egypt. E-mail: Nageh.allam@aucegypt.edu

[b]Department of Analysis and Evaluation, Egyptian Petroleum Research Institute, Cairo, 11727, Egypt

fertilizers in agriculture and the discharge of nitrate-laden industrial effluents. Concentrations as high as 41.6 mM have been reported in industrial wastewater, with textile and groundwater nitrate levels reaching 7.4 mM and up to 1.2 mM, respectively.[14–18] The dual challenge of nitrate remediation and sustainable ammonia production thus renders NO_3RR a promising and impactful target for electrochemical catalysis.

The NO_3RR pathway is mechanistically complex, involving eight-electron and multiple proton-coupled transfer steps:[19–21] $NO_3^- + 6H_2O + 8e^- \rightarrow NH_3 + 9OH^-$. Effective catalysis depends on the adsorption and activation of nitrogenous intermediates and the generation of reactive hydrogen species from water dissociation:[22,23] $H_2O \rightarrow H^* + OH^*$. To achieve high selectivity and activity, electrocatalysts must balance the binding energies of intermediates to suppress side reactions; most notably, the hydrogen evolution reaction (HER) and the formation of nitrite (NO_2^-).[24,25]

Copper (Cu) has emerged as a promising candidate for NO_3RR due to its moderate binding energy for NO_3^-, favorable overpotentials, and compatibility with multi-electron transfer processes.[26–29] Previous investigations demonstrated that structural modifications, such as facet enrichment and roughening of recycled Cu foils, significantly enhanced the exposure of active Cu(100) and Cu(111) sites, leading to improved NO_3^- adsorption, NH_3 yield, and faradaic efficiency (FE).[30] However, these Cu-based systems often suffer from gradual deactivation due to product accumulation and surface poisoning, underscoring the need for improved catalyst designs with enhanced durability.

To overcome these limitations, alloying Cu with zinc (Zn) has been explored as a means of tuning electronic and geometric surface properties while suppressing HER.[31–34] Zn itself is catalytically inactive toward NO_3RR, but when alloyed with Cu, it alters adsorption energetics, enhances stability, and prevents product inhibition through its oxygen-affinitive and proton-repulsive characteristics.[33,34] Brass-based (Cu–Zn) catalysts, in particular, offer an environmentally benign, low-cost platform that has already demonstrated efficacy in related electrocatalytic systems, including CO_2 reduction and water splitting.[32,35–40] Concurrently, new advancements utilizing molecular transition-metal phthalocyanine (TMPc) catalysts have exhibited exceptional efficacy in nitrate reduction. These systems establish clearly defined $M–N_4$ coordination environments that promote charge transfer and stable essential intermediates.[41] Fe-phthalocyanine hollow architectures and Co-phthalocyanine/graphene heterostructures have attained FE% close to 100% while preserving remarkable structural stability, highlighting the significance of π–π stacking and metal–ligand interactions in determining selectivity and reaction kinetics.[42–44] Alignment-controlled Cu- and Fe-phthalocyanine frameworks have demonstrated adjustable electronic architectures that improve NO_3RR selectivity under ambient circumstances. While these molecular systems effectively demonstrate the catalytic benefits of $M–N_4$ motifs, their molecular characteristics and constrained charge-transport pathways limit long-term stability and attainable current densities, underscoring the necessity for durable heterogeneous alternatives such as Cu–Zn alloys.

In this work, we systematically investigate a series of Cu–Zn alloy electrocatalysts (Zn content: 5–50%) for NO_3RR under neutral pH conditions. Neutral electrolytes, while less explored than alkaline counterparts, offer significant advantages for real-world deployment by mitigating corrosive damage, preserving catalyst integrity, and more closely mimicking industrial wastewater environments.[13,45–50] The electrolyte formulation (0.1 M KNO_3 + 0.1 M KCl) was selected to provide stable ionic strength and conductivity while minimizing ohmic losses.[51,52] A unique anodization-annealing method was employed to synthesize phase-stable, structurally defined alloy surfaces, thereby enhancing the exposure of active sites and improving catalyst robustness. Among all tested compositions, $Cu_{85}Zn_{15}$ delivered superior NO_3RR performance, achieving >98% faradaic efficiency and an impressive NH_3 yield rate of 2.8 mmol h^{-1} cm^{-1} at −0.8 V *vs.* RHE. This composition also demonstrated long-term operational stability exceeding 170 hours, far surpassing that of monometallic Cu or other alloyed variants. These findings underscore the potential of Cu–Zn alloys as durable and scalable catalysts for electrochemical ammonia synthesis in neutral media, which were further confirmed *via* DFT calculations.

Experimental details

Preparation of the catalysts

A range of Cu–Zn alloy samples with varying compositions, namely $Cu_{95}Zn_5$, $Cu_{85}Zn_{15}$, $Cu_{70}Zn_{30}$, $Cu_{50}Zn_{50}$, along with pure copper (Cu_{100}) and pure zinc foils, were fabricated following a systematic surface preparation, anodization, and annealing process. Rectangular specimens (30 × 15 × 2 mm) were sectioned using a precision wire saw to maintain consistent geometry. For structural stability and ease of handling, each sample was embedded in a silicone mold with resin prior to surface processing. Surface polishing commenced with sequential abrasion using silicon carbide sandpapers of progressively finer grit sizes, followed by final polishing with alumina slurry to attain a mirror-like finish and alleviate mechanical surface stress. Post-polishing, each specimen underwent ultrasonic cleaning for 10 minutes each in acetone, ethanol, and deionized water to remove surface contaminants. Anodization was conducted in a two-electrode setup using the alloy as the working electrode and a graphite rod as the counter electrode, with a fixed inter-electrode distance of 1.5 cm. The anodization was carried out at room temperature at a constant voltage of 4 V for 5 minutes in an aqueous electrolyte composed of 1 mL of 0.1 M $(NH_4)_2S_2O_8$, 1 mL of 2.5 M NaOH, and 48 mL of DI water. Following anodization, the samples were dried under a nitrogen stream and then annealed under argon flow at 350 °C for 1 hour, employing a ramp rate of 1 °C min^{-1} for both heating and cooling cycles (Fig. 1).

Material characterization

Field-emission scanning electron microscopy (FESEM, TESCAN VEGA COMPACT) was employed to examine the surface morphology of the synthesized alloys. Ultra-high resolution

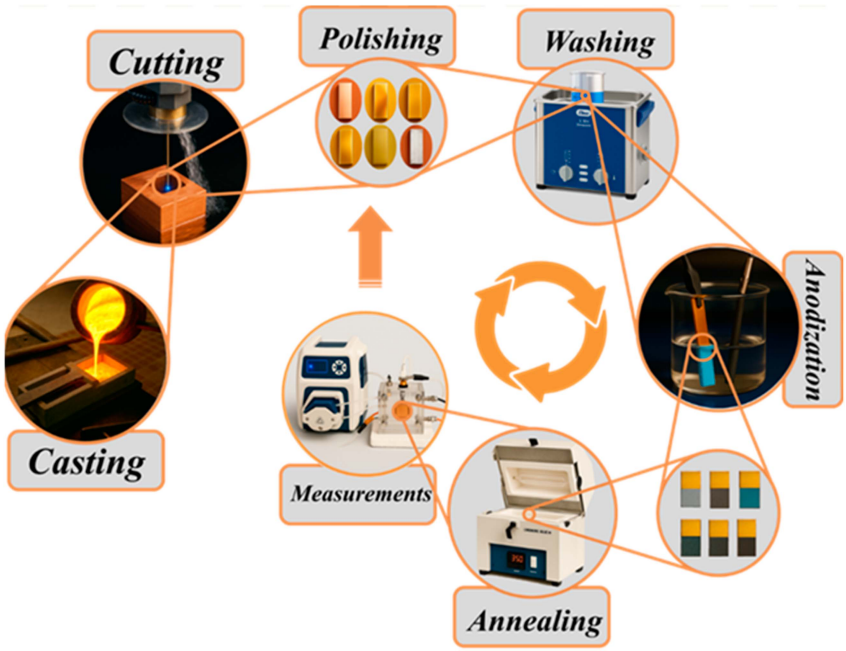

Fig. 1 Schematic illustration of the sample preparation road map. The process begins with casting the metal, cutting, polishing, and washing. Samples then undergo anodization, followed by annealing. The prepared samples are then subjected to electrochemical measurements.

transmission electron microscopy (UHR-TEM) was conducted using a JEM-2100 Plus UHR (JEOL). Elemental analysis was carried out using energy-dispersive X-ray spectroscopy (EDX). X-ray diffraction (XRD) patterns were recorded on a Rigaku MiniFlex 600 diffractometer in the 2θ range of 10–80° with a step size of 0.007°. X-ray photoelectron spectroscopy (XPS) was performed on a Kratos Axis Ultra instrument, with all spectra internally calibrated using the C 1s peak at 284.7 eV. Atomic force microscopy (AFM) measurements were obtained using a Veeco Dimension 3100 instrument to assess surface topography at the nanoscale. Additionally, UV-vis absorption spectra were recorded with a Shimadzu UV-2600i spectrophotometer to evaluate optical properties.

Electrochemical measurements

Electrochemical nitrate reduction tests were performed in a custom-designed, dual-compartment H-type acrylic cell separated by a Nafion 117 membrane. The catholyte chamber was subjected to continuous flow during measurements. A Biologic SP300 potentiostat was used for all electrochemical experiments, with a platinum coil as the counter electrode (CE) and an Ag/AgCl electrode as the reference electrode (RE). A 0.1 M KCl solution served as the supporting electrolyte for both compartments. Prior to testing, the system was purged with ultra-high-purity N_2 (99.9999%) for 30 minutes. For nitrate reduction experiments, 0.1 M KNO_3 was added to the catholyte. All measured potentials were converted to the RHE scale using the equation: $E_{RHE} = E_{Ag/AgCl} + 0.1976 + 0.059pH$. Electrochemical tests were carried out using electrodes with a geometric area of 1 cm^2. Chronoamperometry was performed for 1 hour over a potential range from 0 to −0.8 V *vs.* RHE. Linear sweep voltammetry (LSV) was conducted from 0.45 to −0.8 V *vs.* RHE at a scan rate of 10 mV s^{-1}. Cyclic voltammetry (CV) was conducted at varying scan rates (20–120 mV s^{-1}) in a non-faradaic potential window to estimate the electrochemical double-layer capacitance (C_{dl}), determined *via* $\Delta J = (J_{anodic} - J_{cathodic})/2$ plotted against scan rate. The electrochemical active surface area (ECSA) was further evaluated using C_{dl}, underpotential deposition (UPD) techniques, and electrochemical impedance spectroscopy (EIS). EIS measurements were performed at the working potential over a frequency range from 100 kHz to 10 mHz. A schematic of the electrochemical setup is shown in Fig. S1.

Results and discussion

Catalyst design and surface engineering

Cu–Zn alloy catalysts were synthesized *via* anodization followed by thermal annealing for one hour at 350 °C in an argon atmosphere. This post-treatment strategy effectively promotes the formation of stable phases.[35] The selected annealing temperature balanced complete dehydration and prevention of Cu_2O overoxidation to CuO. Zinc (Zn), on the other hand, was consistently oxidized to ZnO without significant structural transformation.[38]

X-ray diffraction (XRD) analysis (Fig. 2a) revealed strong reflections at $2\theta = 43.3°$, 50.4°, and 74.1°, corresponding to the (111), (200), and (220) planes of FCC Cu (COD no. 96-901-3018), confirming metallic copper as the dominant bulk phase. The minor peak at 36.5° matched the (111) plane of Cu_2O (COD no. 96-900-5770). In the context of Rietveld refinement, the percentages of the two phases were determined to be 1.4 for Cu and 0.03 for Cu_2O in mass in the $Cu_{85}Zn_{15}$ sample, which is

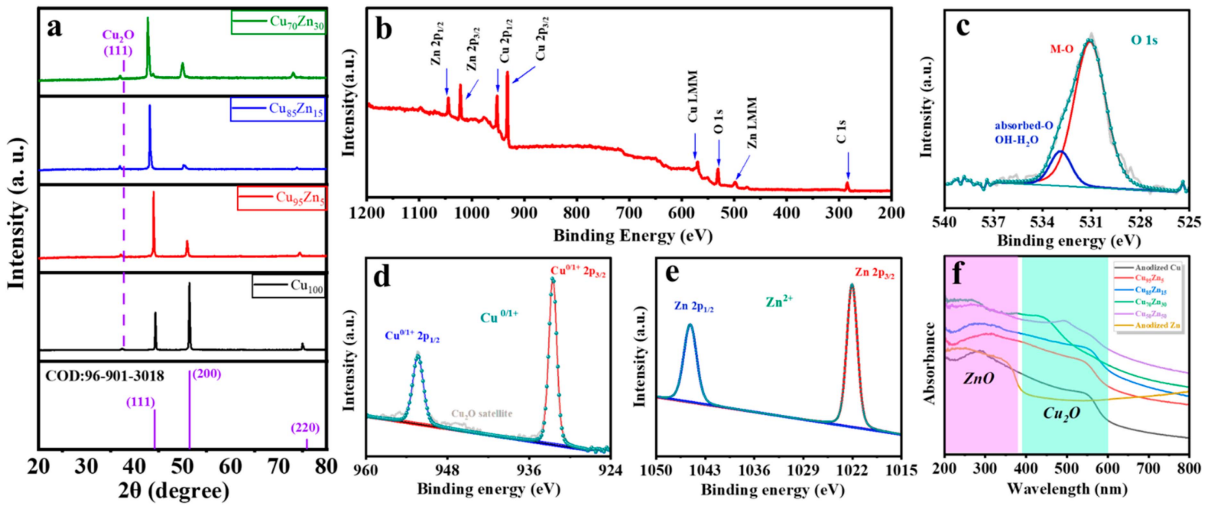

Fig. 2 (a) XRD spectra of the catalysts, XPS (b) survey (c) Cu 2p, (d) Zn 2p, (e) O 1s spectra, and (f) UV-vis spectra of the Cu–Zn catalysts.

consistent with the data obtained using Jana 2006 software. No reflection peaks were detected for CuO. The lack of crystalline ZnO peaks suggested either a high dispersion or incorporation of Zn into the Cu lattice. Shifts in the Cu_2O peak to lower 2θ values indicated substitutional doping, consistent with Vegard's law.[53] These results align with the Cu–Zn phase diagram (Fig. S2), which predicts single-phase α-brass below ~35 wt% Zn.[35,38,54] Crystallite sizes calculated using the Debye–Scherrer equation were 49.08 nm (Cu), 45.98 nm ($Cu_{95}Zn_5$), and 23.12 nm ($Cu_{85}Zn_{15}$), indicating that moderate Zn incorporation may restrict grain growth due to lattice strain or defects. Moreover, XRD analysis of the $Cu_{50}Zn_{50}$ catalyst was performed to identify the phase composition. As shown in Fig. S3, the diffraction peaks at $2\theta \approx 43.6°$, 62.7°, and 79.54° correspond to the (110), (200), and (211) planes of the β-Cu–Zn phase, in agreement with the Cu–Zn phase diagram prediction near the equiatomic composition. Minor peaks at 31.7°, 36.9°, and 39.2° are attributed to ZnO_2(111), Cu_2O(111), likely due to slight surface oxidation, and Zn(100), respectively. Although XRD revealed the bulk and surface crystalline phases, it limits the resolution necessary to differentiate the surface oxidation states of copper and zinc species. Therefore, X-ray photoelectron spectroscopy (XPS) was employed to reveal the surface chemical states of the $Cu_{85}Zn_{15}$ catalyst (Fig. 2b–e). Cu 2p peaks at 932.5 eV (Cu $2p^{3/2}$) and 952.3 eV (Cu $2p^{1/2}$) with a spin–orbit splitting of 19.8 eV, corresponding to Cu/Cu_2O, confirm the presence of Cu^0 and/or Cu^+.[45,55,56] The absence of shake-up satellite peaks in the 940–945 eV range indicates the absence of Cu^{2+}. Zn 2p spectra showed peaks at 1022.05 eV and 1045.13 eV with a spin–orbit coupling of 23.1 eV, consistent with Zn^{2+} species in ZnO.[57] The O 1s signal had components at 531.07 eV (lattice oxygen) and 532.79 eV (hydroxyls/water).[58] From the survey spectrum (Fig. 2b), the Cu $2p_3/_2$ peak is located at 932.5 eV, and the Cu LMM Auger peak (binding energy 568.0 eV) corresponds to a kinetic energy of 918.6 eV. The resulting modified Auger parameter is $\alpha' = 932.5 + 918.6 = 1851.1$ eV, which matches the literature value for metallic Cu^0 (1851.24 eV (ref. 59)), thereby conclusively assigning the copper oxidation state as zero. UV-vis absorption spectroscopy (Fig. 2f) confirmed the coexistence of ZnO (UV absorption near 360 nm, bandgap ~ 3.4 eV) and Cu_2O (visible absorption at ~500–600 nm, bandgap ~ 2.0 eV).[60–62] The Pourbaix diagram (Fig. S4) further supports that Zn oxidizes preferentially under the applied potentials, stabilizing Cu in reduced states.[55] Additionally, EDX analysis was performed after the annealing treatment, and the elemental ratios remained nearly identical to those obtained before any treatment, as shown in Fig. S9 and Table S2. Furthermore, EDX analysis of the $Cu_{85}Zn_{15}$ catalyst after the electrochemical reaction also showed comparable Cu/Zn ratios, confirming the structural and compositional stability of the catalyst during the reaction (Fig. S10). Furthermore, the TEM images of the $Cu_{85}Zn_{15}$ alloy (Fig. 3e) display a porous, interconnected nanostructure comprised of nanoparticles, offering an extensive surface area for electrochemical activity. The contrast between dark and light sections reflects compositional heterogeneity; the darker regions represent copper, and the lighter regions indicate zinc. The selected area electron diffraction (SAED) pattern in (Fig. 3f) corroborated the diffraction characteristics of (111), (200), (220), and (311) planes of metallic Cu, as well as extra rings corresponding to Cu_2O, thereby verifying the coexistence of Cu^0/Cu^+ phases. Following the nitrate reduction reaction, morphology was predominantly maintained, demonstrating exceptional structural stability under operational conditions. The SAED pattern exhibited consistent Cu and Cu_2O reflections, with no emergence of new diffraction spots (Fig. S11), thereby confirming the absence of phase transformation or Zn segregation during electrolysis. Topographical features were explored using atomic force microscopy (AFM) for all compositions (Fig. S12). The AFM image in (Fig. 3g) reveals nanoscale protrusions on $Cu_{85}Zn_{15}$, attributed to Zn incorporation, which likely improves interfacial reactivity and nitrate adsorption.[63] The roughness factor (RF) was highest for $Cu_{85}Zn_{15}$ (RF = 30.2), with excess Zn (>15%) found to reduce RF due to disrupted surface patterning, see (Table S3).

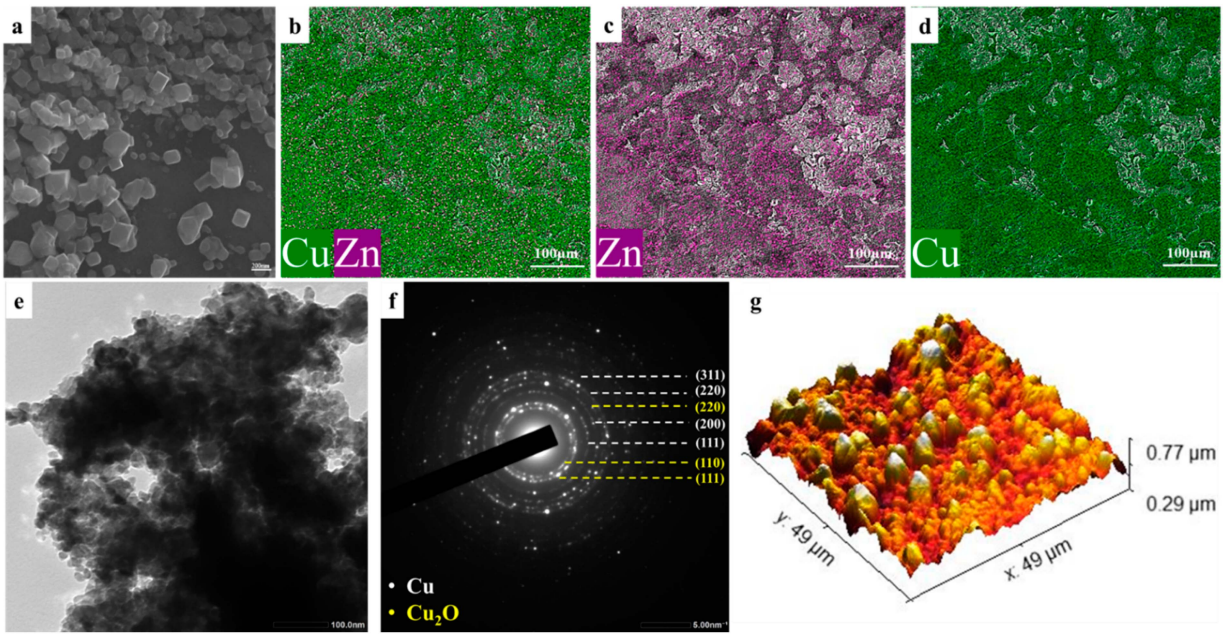

Fig. 3 (a) SEM image, (b–d) EDX elemental mapping of Cu and Zn, (e) HRTEM image, (f) SAED pattern confirming the presence of Cu and Cu_2O phases, and (g) 3D AFM surface morphology illustrating surface roughness distribution of the $Cu_{85}Zn_{15}$ catalyst.

Electrochemical performance

To investigate the electrochemical performance of catalysts towards nitrate reduction, linear sweep voltammetry (LSV) experiments were performed in the absence (0.1 M KCl) and presence (0.1 M KNO_3 + 0.1 M KCl) of nitrate ions (Fig. 4a). LSV curves recorded in nitrate-containing and nitrate-free electrolytes confirmed that current response was driven by NO_3^- electroreduction. The $Cu_{85}Zn_{15}$ catalyst showed the highest current density and the most favorable onset potential, outperforming pure Cu and other catalyst variants. Notably, the cathodic peak at ~−0.45 V *vs.* RHE, usually observed in pure Cu disappeared upon Zn addition, suggesting a modified intermediate binding,[64] indicating that $Cu_{85}Zn_{15}$ offers reasonable performance for selective nitrate to ammonia conversion under neutral conditions. The ammonia concentration was quantified using the blue indophenol method with a standard calibration

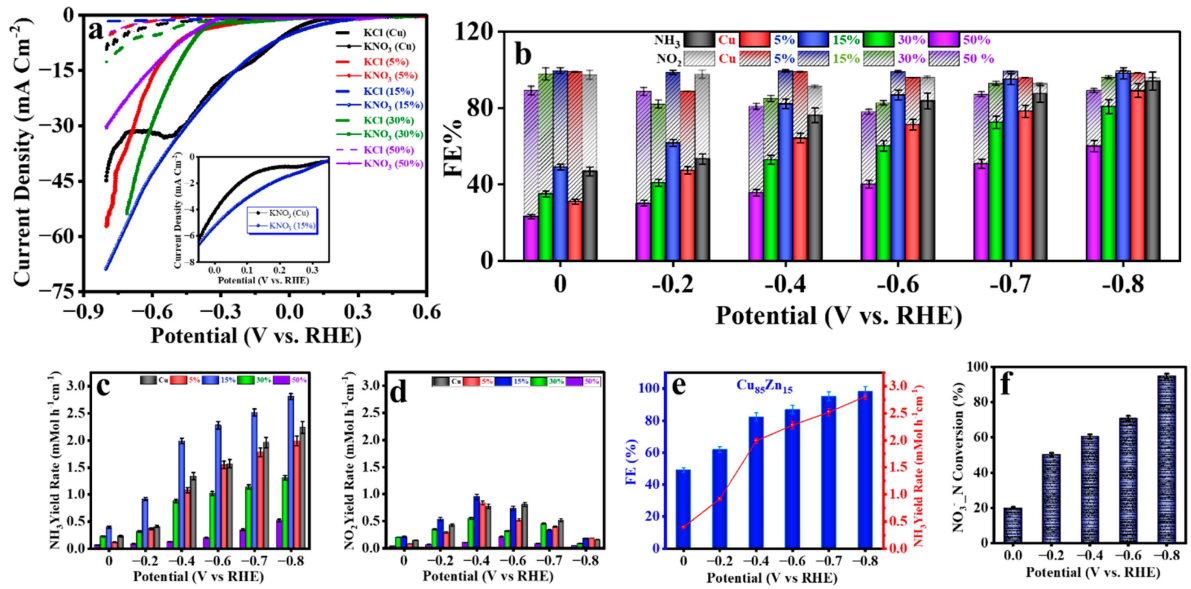

Fig. 4 (a) LSV curves recorded in 0.1 M KCl electrolyte "dashed line" and in 0.1 M KCl + 0.1 M NO_3^- mixed electrolyte "solid line" for all catalysts, (b) FE of NH_3 and NO_2 for all catalysts, (c) NH_3 yield rate and (d) NO_2^-, (e) FE and YR for the $Cu_{85}Zn_{15}$ catalyst, and (f) the NO_3^-–N conversion for the $Cu_{85}Zn_{15}$ catalyst.

curve (Fig. S13).[65] This electrocatalytic behavior was verified by evaluating the faradaic efficiency (FE) and NH_3 production yield rate (YR) for all catalysts over a wide applied potential range (0 to −0.8 V *vs.* RHE) as depicted in Fig. 4b and c. $Cu_{85}Zn_{15}$ exhibited a FE of ∼98% for NH_3 at −0.8 V *vs.* RHE, with a yield rate of ∼2.8 mmol h^{-1} cm^{-2}. Hydrogen quantification experiments were performed in a closed H-cell. Gas samples were collected from the headspace and analysed using GC. The integrated H_2 peak area was approximately 30, which is near the lower limit of our calibration range (Fig. S14). To further validate this observation, we continuously monitored the headspace using a portable gas analyser (GeoTech, UK),[66,67] which consistently recorded an average H_2 concentration of ∼25 ppm over the course of 1 hour of electrolysis. Importantly, these measurements were repeated in three independent trials, yielding highly reproducible results. Together, these findings confirm that H_2 production in our system is minimal, consistent with our faradaic balance calculations (FE% NH_3 = 98%), and support the conclusion that the hydrogen evolution reaction (HER) is strongly suppressed on Cu–Zn alloys under our neutral H-cell operating conditions. By contrast, Cu and $Cu_{95}Zn_5$ showed lower FE (∼94% and 90%) and YR (∼2.2 and 1.9 mmol h^{-1} cm^{-2}). Higher Zn content (*e.g.*, $Cu_{70}Zn_{30}$ and $Cu_{50}Zn_{50}$) significantly reduced both FE and YR, likely due to dezincification and HER competition.[38] Byproduct NO_2^- selectivity was highest at mid-potentials (−0.2 to −0.4 V) for suboptimal alloys, whereas $Cu_{85}Zn_{15}$ consistently suppressed NO_2^- formation (Fig. 4d and e). The quantification of nitrite byproducts was performed using a standard calibration curve (Fig. S15). NO_3^--N conversion efficiency reached ∼96% for $Cu_{85}Zn_{15}$ at −0.8 V (Fig. 4f), indicating efficient nitrate utilization. Additionally, residual nitrate concentrations were determined using a UV-vis calibration curve (Fig. S16). Compared to reported Cu-based systems (Table 1), $Cu_{85}Zn_{15}$ offers superior performance using a neutral electrolyte without noble metals or harsh conditions. Although our catalyst is cost-effective, it delivers remarkable faradaic efficiency and an unprecedented ammonia yield rate in a neutral KNO_3 electrolyte system (0.1 M KNO_3 + 0.1 M KCl). Consequently, the $Cu_{85}Zn_{15}$ system, distinguished by its exceptional simplicity, emerges as a low-cost, resource-efficient solution for selective nitrate electroreduction, with strong potential for industrial-scale deployment in the near future. The catalytically active sites were identified as dynamic Cu^0/Cu^+–ZnO heterointerfaces, which were formed during the nitrate reduction reaction (NO_3RR) under negative potentials. In these conditions, nitrate was reduced to ammonia while surface copper oxides were decreased dynamically, resulting in a stable mixture of metallic Cu (Cu^0) and Cu(I) (Cu_2O) without detectable Cu^{2+} species. This assignment was supported by XPS analysis, in which clear Cu^0/Cu^+ features were observed without shake-up satellites characteristic of Cu^{2+}. The role of Zn was established as crucial for maintaining this interfacial stability, since Zn was preferentially oxidized to ZnO, thereby preventing excessive oxidation of Cu and modifying the local electronic environment to suppress the competing HER. Such synergistic effects at Cu–ZnO have also been reported in the literature,[68] where enhanced NO_3RR performance was attributed to interfacial electronic interactions and HER suppression. Collectively, our experimental evidence (XRD, XPS, UV-vis) and prior mechanistic studies indicate that the active phase in the Cu–Zn catalysts can be best described as dynamically formed Cu^0/Cu^+ surface.

Surface characterization and active site analysis

To gain deeper insight into the surface characteristics of the Cu–Zn alloy catalysts, the electrochemically active surface area (ECSA) was evaluated using cyclic voltammetry (CV) in the non-faradaic potential region at varying scan rates (Fig. S17). Among the tested samples, $Cu_{85}Zn_{15}$ exhibited the highest ECSA, as calculated using eqn (S5), surpassing that of pure Cu and $Cu_{95}Zn_5$ by approximately 26.5% and 47.7%, respectively (Fig. 5a). These findings are consistent with atomic force microscopy (AFM) measurements, which revealed a surface roughness factor (RF) of 30.2 for $Cu_{85}Zn_{15}$, the highest among

Table 1 Comparison of the performance of our developed materials with those documented in the literature for Cu-based electrocatalysts in the nitrate reduction reaction (NO_3RR)

Material	Electrolyte	(FE%)	NH_3 yield rate (mmol h^{-1} cm^{-2})	ECSA (cm^2)	Stability	Potential (V *vs.* RHE)	Ref.
Cu–Sn bimetallic alloy	0.1 M Na_2SO_4 + 0.01 M $NaNO_3$	78.57%	0.2931	—	26 h	−1.20 V	81
Cu@Ni tandem catalyst	1 M KOH + 0.1 M KNO_3	92.5%	0.2254	62.5	—	−0.20 V	82
Fe–N–C	0.05 M PBS + 0.16 M KNO_3	99.1	0.010	—	6 h	−0.40 V	83
$Cu_{50}Ni_{50}$/PTFE alloy catalysts	1 M KOH + 0.1 M KNO_3	99 ± 1%	—	61.25	12 h	−0.15 V	84
TpBpy–Cu–F	0.5 M $NaNO_3$ + 0.5 M Na_2SO_4	92.7%	0.876	27.3	5 h	−0.83 V	85
Cu–Pd/C nano belts	0.1 M KOH + 0.01 M KNO_3	62.3%	0.013	0.76	26 h	−0.40 V	64
Fe/Cu-HNG	1.0 M KOH + 0.1 M KNO_3	92.5%	0.54	—	24 h	−0.30 V	18
M–Cu/Cu_2O	1 M KOH + 0.1 M KNO_3	95%	0.25	140	20 h	−0.20 V	86
Cu(100)-rich foil	0.1 M K_2SO_4 + 0.014 M KNO_3	98%	1.1	6.87	100 h	−0.55 V	87
Recycled copper sheets	0.1 M KCl + 0.1 M KNO_3	97.6%	2.162	6.5	20 h	−0.80 V	30
Cu@ZnO NWA	0.1 M KOH + 0.05 M KNO_3	89.14%	0.354	278	100 h	−0.60 V	68
Pd Cu/Cu_2O hybrids	0.5 M Na_2SO_4 + 100 ppm NO_3^-–N	94.32%	0.190	10.1	12 h	−0.80 V	88
Cu–Zn alloy	0.1 M KCl + 0.1 M KNO_3	98%	2.8	200.1	170 h	−0.8 V	This work

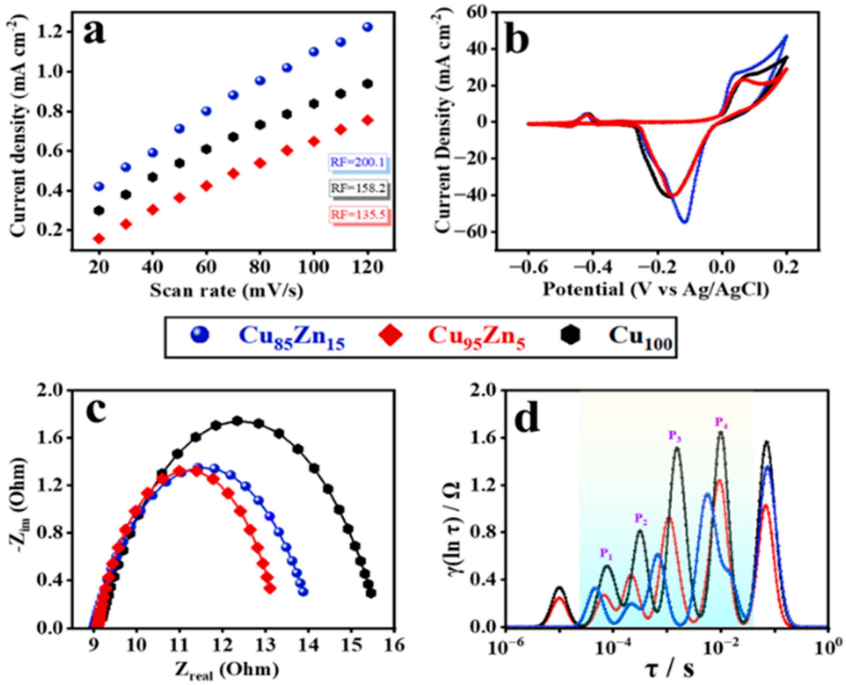

Fig. 5 (a) C_{dl} curves for ESCA calculation along with the extrapolated roughness factor values; (b) Pb underpotential deposition (Pb-UPD), (c) Nyquist plots from EIS measurements; (d) distribution of relaxation times (DRT) analysis for $Cu_{85}Zn_{15}$ (blue), $Cu_{95}Zn_5$ (red), and pure Cu (black) sample.

the examined catalysts. To further confirm the electrochemically accessible surface area, underpotential deposition of lead (UPD-Pb) was employed as a selective surface probe.[69] The stripping voltammograms (Fig. 5b) showed significantly greater Pb coverage on $Cu_{85}Zn_{15}$, with an RF-Pb of 8.95, compared to 6.02 for $Cu_{95}Zn_5$ and 6.57 for pure Cu. The higher Pb deposition indicates a dense population of active sites, which likely contributes to the enhanced nitrate-to-ammonia conversion efficiency observed for $Cu_{85}Zn_{15}$.[70] The combined evidence from ECSA, AFM, and UPD-Pb analyses strongly supports that incorporating ~15% Zn into Cu catalysts optimizes surface morphology and maximizes the density of electrochemically active sites, thereby improving catalytic performance. To further elucidate the interfacial properties of the catalysts, electrochemical impedance spectroscopy (EIS) was employed. EIS is a highly sensitive diagnostic technique that provides detailed information on surface characteristics, interfacial charge transfer, and capacitive behavior in electrochemical systems.[71,72] Surface heterogeneities, such as physical roughness or compositional inhomogeneity, can perturb the double-layer structure, and these effects are often detectable through characteristic frequency-dependent responses in EIS measurements.[73] In metallic electrodes, charge transfer occurs primarily through free electrons, with negligible contribution from ionic diffusion due to the dense atomic structure and strong metallic bonding.[74] As such, EIS measurements during the electrochemical nitrate reduction reaction (NO_3RR) can yield critical insights into catalytic activity and interfacial kinetics.[30] Interestingly, EIS analysis (Fig. 5c) revealed lower charge transfer resistance (R_{CT}) for $Cu_{85}Zn_{15}$, with fitted Nyquist plots matching a Randle's-type circuit lacking a Warburg element, consistent with fast NO_3^- diffusion and rapid transport kinetics.[75] The CPE exponent values (α), which quantify the deviation from ideal capacitive behavior, ranged from 0.6381 to 0.7107, indicative of moderate surface inhomogeneity. The double-layer capacitance (C_{dl}) was derived from the fitted CPE parameters using eqn (S7).[73] Among all compositions, $Cu_{85}Zn_{15}$ exhibited the highest effective capacitance (CCPE = 0.02062 F), corresponding to a significant enhancement in electrochemically active surface area compared to pure Cu and $Cu_{95}Zn_5$.

These EIS-derived capacitance values are consistent with trends observed in AFM, ECSA, and UPD-Pb measurements (Table 2), further reinforcing the superior surface accessibility and capacitive behavior of $Cu_{85}Zn_{15}$. This correlation underscores the crucial role of optimal Zn incorporation in enhancing the electrochemical interface and facilitating efficient nitrate reduction. Following impedance measurements, the Distribution of Relaxation Times (DRT) analysis was employed to better understand the fundamental electrochemical processes by separating them over several time frames.[76] The time range of

Table 2 Roughness factor (RF) of the investigated catalysts estimated from various techniques

Sample	RF from AFM	RF from ECSA	RF from UPD-Pb	CCPE (F)
Pure Cu	27.7	158.2	6.57	0.0061
$Cu_{95}Zn_5$	20.1	135.5	6.02	0.0057
$Cu_{85}Zn_{15}$	30.2	200.1	8.95	0.0206

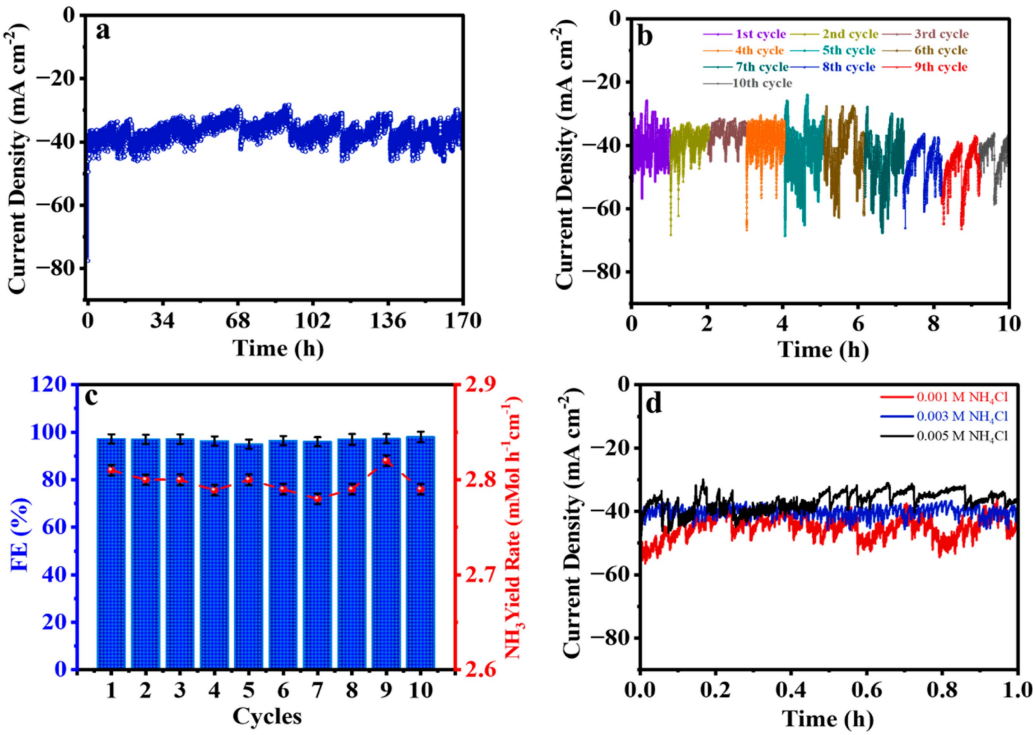

Fig. 6 (a) Stability test for 170 h in $Cu_{85}Zn_{15}$ electrode; (b) cycling stability over 10 consecutive tests; (c) faradaic efficiency (FE) and ammonia yield rate (YR) stability across cycles; (d) chronoamperometry curve at different NH_4Cl concentrations (0.001, 0.003, and 0.005 M) for $Cu_{85}Zn_{15}$.

(10^{-6} to 10^{-5} s) refers to rapid electrical reactions, including contact resistance and electrode conductivity, with minor peaks signifying favorable electronic conductivity throughout all samples.[77] In the resistive-capacitive region (10^{-4} to 10^{-2} s), the DRT profiles of Cu, $Cu_{95}Zn_5$, and $Cu_{85}Zn_{15}$ (Fig. 5d) show multiple peaks, which indicate the existence of sequential interfacial processes. In detail, P1 is attributed to electron transport from the bulk to the surface, P2 to surface adsorption and restructuring, P3 to double-layer formation at the electrode/electrolyte interface, and P4 to charge transfer to adsorbed nitrate species during NO_3RR. Note that the number of peaks is similar across all samples, but the peak intensities differ. For each sample, the highest peak corresponds to the dominant resistive process. For example, P4 is the most intense in pure Cu, which indicates that R_{CT} is higher, and reaction kinetics is slower. On the contrary, $Cu_{85}Zn_{15}$ shows a lower P4 intensity, which reflects both reduced R_{CT} and faster charge transfer. The observed enhancement may be ascribed to the incorporation of Zn, which modifies the surface structure, improves active site availability, and facilitates more efficient electron transfer during nitrate reduction. Thus, the intensity of P4 refers to the R_{CT} of NO_3RR, while its lower intensity in $Cu_{85}Zn_{15}$ implies reduced R_{CT} and enhanced kinetics, explaining the better electrochemical performance for $Cu_{85}Zn_{15}$ than pure Cu.[78] In the long-term domain (10^{-1} to 1 s), commonly linked to mass transport constraints, the persistent DRT response suggests effective ionic diffusion and maintained electrochemical activity.[79,80] To probe whether increasing NH_3 concentrations in the electrolyte would inhibit catalyst activity, a common issue due to product accumulation, we performed an additional series of electrolysis experiments in which nitrate was partially substituted with ammonium chloride (NH_4Cl) at concentrations of 0.01, 0.03, and 0.05 M, while keeping the total salt concentration constant at 0.1 M. As shown in (Fig. 6b), the current response remained steady even at higher NH_3 levels, suggesting that product accumulation does not block active sites on the catalyst surface. This finding confirms that $Cu_{85}Zn_{15}$ is tolerant to elevated ammonia concentrations and does not suffer from product inhibition.

Catalytic performance was further monitored through UV-vis spectroscopy at various time intervals (6, 10, 12, 24, 48, and 72 hours). The consistent ammonia signals confirmed sustained catalytic activity and reinforced the catalyst's structural integrity under extended electrochemical operation. Additionally, a short-term kinetic study was conducted under continuous electrolysis for 2 hours, with solution sampling every 10 minutes. As depicted in (Fig. S18), the gradual increase in absorption signal in the wavelength range of 630–700 nm indicated continuous NH_3 generation, supporting the catalyst's effective activity under operational conditions.

Stability and reusability

To evaluate the long-term durability of the $Cu_{85}Zn_{15}$ catalyst under continuous operation, chronoamperometric measurements were performed at −0.8 V *vs.* RHE for 170 hours in 0.1 M KNO_3 + 0.1 M KCl electrolyte (Fig. 6a). Electrolysis was conducted under a cyclic solution replacement protocol, with the nitrate-containing electrolyte refreshed every 24, 48, or 72 hours

to simulate practical scheduling flexibility in industrial operations. This configuration mimics semi-batch industrial processes, in which partial product extraction is followed by solution recirculation. In our setup, a single beaker served both as the feed and collection vessel to replicate this operating mode. The $Cu_{85}Zn_{15}$ catalyst exhibited stable current density throughout the entire test period, with no noticeable degradation in performance, highlighting its robust operational stability. To assess reusability, $Cu_{85}Zn_{15}$ was subjected to ten consecutive NO_3^- reduction cycles at −0.8 V *vs.* RHE. As shown in (Fig. 6c), both the faradaic efficiency (FE) and NH_3 yield rate remained stable across all cycles. Current–time (*i–t*) profiles (Fig. 6d) also showed negligible variation in current density, confirming the catalyst's electrochemical stability and the absence of structural degradation, as confirmed *via* the SEM imaging (Fig. S19) and XRD investigation (Fig. S20) of the $Cu_{85}Zn_{15}$ catalyst after stability testing. These results demonstrate that the $Cu_{85}Zn_{15}$ catalyst can be reused multiple times without performance loss due to undesirable surface passivation or deactivation, as confirmed *via* XPS analysis (Fig. S21).

To ensure that the detected ammonia originated solely from electrochemical nitrate reduction and not from contamination or background electrolyte, a series of control experiments were conducted (Fig. S22). Open circuit potential (OCP) tests in both 0.1 M KCl and 0.1 M KNO_3 revealed negligible UV-vis absorbance (<0.001 a.u. in the 630–700 nm region), indicating no NH_3 generation under non-electrolytic conditions. Furthermore, electrolysis in nitrate-free 0.1 M KCl electrolyte at −0.8 V *vs.* RHE for 1 hour produced a minimal signal, while post-electrolysis analysis of the anode revealed no detectable NH_3. These control studies confirm that the ammonia signals recorded during electrolysis in nitrate-containing media were exclusively due to the electrochemical nitrate reduction reaction (NO_3RR) and not experimental artifacts or contamination.

To elucidate the superior performance of the $Cu_{85}Zn_{15}$ alloy in nitrate electroreduction compared to pure Cu, $Cu_{95}Zn_5$, and $Cu_{70}Zn_{30}$, we conducted density functional theory (DFT) calculations, employing the (111) surface based on our experimental characterizations.[89] All DFT calculations were performed using VASP 5.4.4 with the PBE functional and ultrasoft pseudopotentials. A plane-wave cutoff of 550 eV and a 3 × 3 × 1 Monkhorst–Pack *k*-point mesh was employed. The Cu and Cu–Zn alloy (111) surfaces were modeled as 3 × 3 supercells with 20 Å vacuum spacing. The convergence thresholds were 5 × 10–6 eV per atom for electronic relaxation and 0.01 eV $Å^{-1}$ for ionic forces. Free energies were computed using the computational hydrogen electrode approach, including zero-point energy and entropic corrections, and solvation effects were assessed with the VASPsol implicit solvent model. Detailed equations are provided in the SI.

Pure Cu is prone to catalyst poisoning due to the strong binding of $*NO_x$ species, which hampers their protonation and consequently impedes further reaction steps. Excessive $*NO_x$ adsorption blocks active sites and lowers catalytic activity. An ideal catalyst for the nitrate reduction reaction (NO_3RR) must therefore balance $*NO_x$ adsorption with facile protonation of intermediates, governed by the selective stabilization of key species along the reaction pathway.

We began by evaluating the adsorption behavior of NO_3^-, a critical initial step in NO_3RR. On the CuZn(111) surface, NO_3^- adopts a side-on adsorption mode through two oxygen atoms and binds at several distinct bridge sites: Cu–Zn (BCuZn), Cu–Cu (BCuCu), and Zn–Zn (BZnZn). On the $Cu_{85}Zn_{15}(111)$ surface, the adsorption energies (E_{*NO_3}) at these sites are −0.52 eV (BCuZn), −0.18 eV (BCuCu), and −0.42 eV (BZnZn), all indicating thermodynamically favorable interactions. Notably, adsorption at the BCuZn site is most favorable and substantially stronger than on pure Cu (−0.04 eV), identifying it as the primary active site. Here, NO_3^- undergoes significant structural distortion, with elongated N–O bonds and a compressed O–N–O angle of 117.44°, likely driven by the short Cu–Zn bond length that enhances electron delocalization and bond weakening.

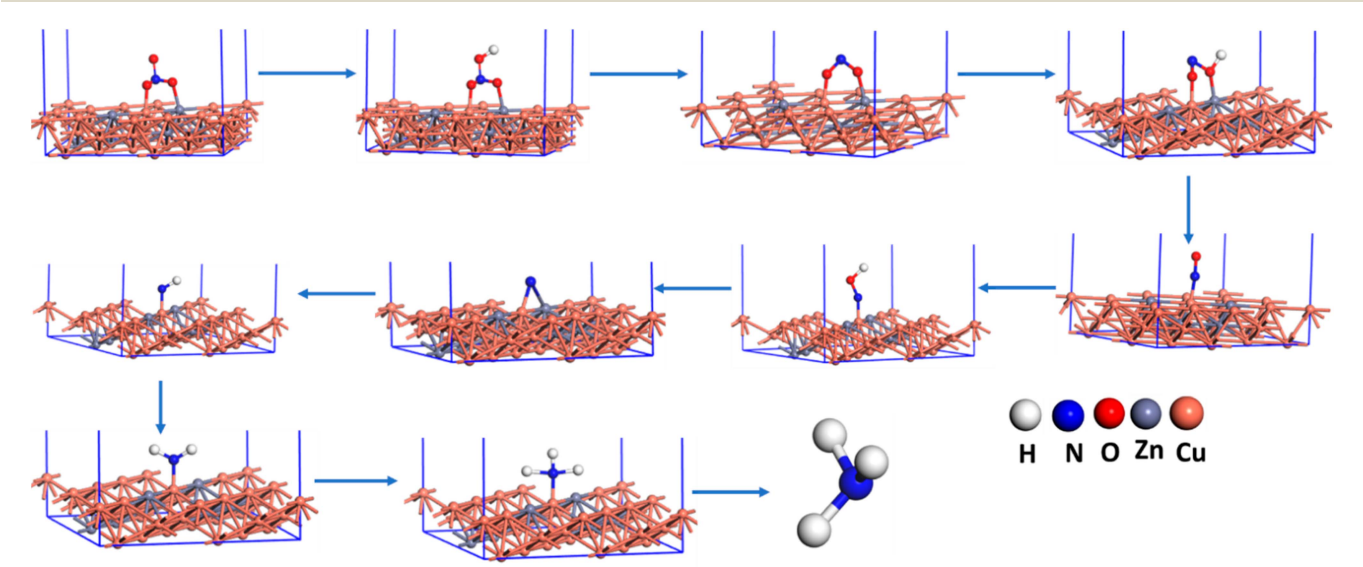

Fig. 7 The least energy pathway to NH_3 as the predominant product.

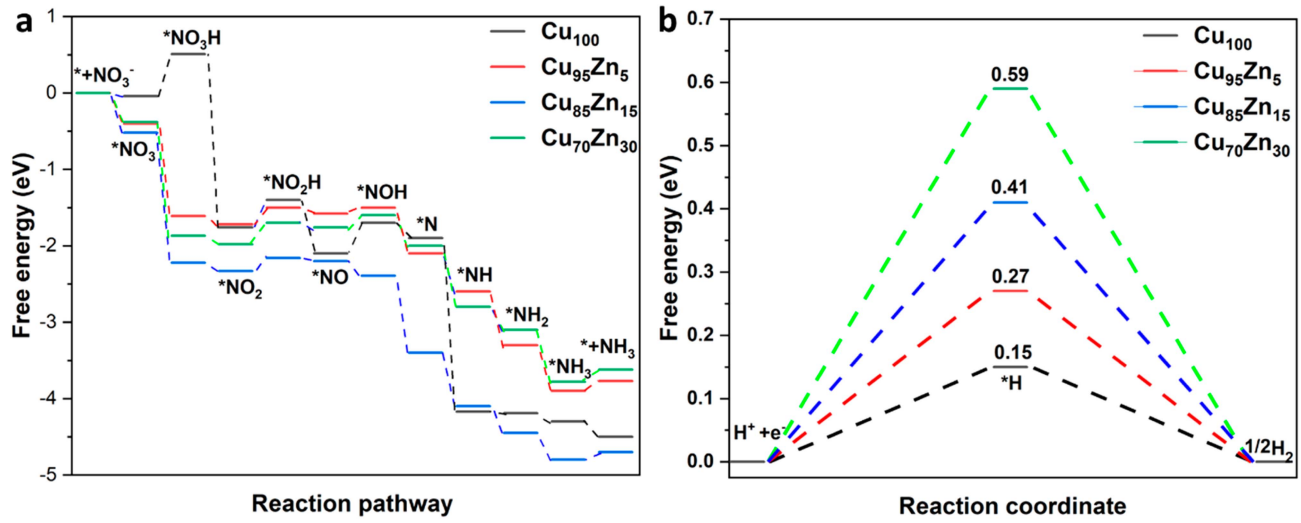

Fig. 8 (a) NRR energy diagram and (b) HER diagram for Cu_{100}, $Cu_{95}Zn_5$, $Cu_{85}Zn_{15}$, and $Cu_{70}Zn_{30}$ catalysts.

The overall NO_3RR to NH_3 involves the transfer of nine protons and eight electrons, beginning with a solution-mediated protonation of NO_3^- to form HNO_3, without direct electron transfer (see SI for full equations). The full reaction mechanism and intermediate structures are shown in (Fig. 7). To assess the catalytic efficiency, we computed the reaction free energies (ΔG) for the key $*NO_3 \rightarrow *NO_3H$ step on Cu(111), $Cu_{95}Zn_5$(111), $Cu_{85}Zn_{15}$(111), and $Cu_{70}Zn_{30}$(111) surfaces. The ΔG values are 0.51, −1.61, −2.22, and −1.87 eV, respectively, indicating significantly more favorable kinetics on the Cu–Zn alloy surfaces, especially $Cu_{85}Zn_{15}$ (Fig. 8a). Subsequent hydrogenation of $*NO_2$ proceeds *via* H^+/e^- attack on the oxygen atoms to form $*NO_2H$. The adsorption energies for $*NO_2H$ are 0.36, 0.22, 0.17, and 0.28 eV for Cu(111), $Cu_{95}Zn_5$(111), $Cu_{85}Zn_{15}$(111), and $Cu_{70}Zn_{30}$(111), respectively. On $Cu_{85}Zn_{15}$, the $*NO_2$ intermediate exhibits an elongated N–O bond (~1.26 Å), facilitating bond weakening and easier hydrogenation. The rate-determining step (RDS) on Cu–Zn surfaces is the protonation of $*NO_2$, with a remarkably low energy barrier of 0.17 eV for $Cu_{85}Zn_{15}$. Conversely, on pure Cu, the RDS is the protonation of $*NO_3$, with a higher barrier of 0.55 eV. Moreover, Cu–Zn alloys suppress the competing hydrogen evolution reaction (HER), with HER barriers of 0.27, 0.41, and 0.59 eV for $Cu_{95}Zn_5$, $Cu_{85}Zn_{15}$, and $Cu_{70}Zn_{30}$, respectively (Fig. 8b).

Conclusions

In summary, the Cu–Zn alloy catalysts developed in this study demonstrate significant promise for the electrochemical reduction of nitrate to ammonia under neutral pH conditions. Among the investigated compositions, $Cu_{85}Zn_{15}$ exhibited the most favorable performance, achieving a faradaic efficiency of approximately 98% and an ammonia yield rate of 2.8 mmol h^{-1} cm^{-2}. Comprehensive surface analyses, including AFM-derived roughness factor (RF), electrochemically active surface area (ECSA) *via* cyclic voltammetry, and underpotential deposition of Pb-confirmed that the enhanced catalytic activity stems from an increased density of electrochemically accessible active sites. The $Cu_{85}Zn_{15}$ catalyst maintained its performance over 170 hours of continuous operation and remained structurally and functionally stable over ten reuse cycles under simulated recirculation conditions. These durability metrics, combined with high selectivity and productivity, underscore the robustness of the catalyst. Compared to previously reported Cu-based systems, $Cu_{85}Zn_{15}$ offers superior efficiency, long-term stability, and cost-effective synthesis, making it a highly competitive candidate for scalable and sustainable ammonia production. DFT calculations revealed that the $Cu_{85}Zn_{15}$ alloy exhibits optimal $*NO_3^-$ adsorption and significantly lowers energy barriers for key protonation steps, particularly at the Cu–Zn bridge sites, thereby enhancing NO_3RR activity. The alloy also suppresses the competing hydrogen evolution reaction and facilitates favorable intermediate stabilization, collectively accounting for its exceptional selectivity and catalytic efficiency in neutral media. Overall, these findings establish $Cu_{85}Zn_{15}$ as an optimal electrocatalyst for low-carbon, energy-efficient conversion of nitrate-laden wastewater into ammonia, addressing both environmental remediation and green nitrogen-cycle integration.

Conflicts of interest

There are no conflicts to declare.

Data availability

The data supporting this article have been included as part of the supplementary information (SI). Supplementary information: preparation of the catalysts, materials, and reagents, materials characterization, electrochemical measurements, determination of ion concentration, computational details, and involved calculations. See DOI: **https://doi.org/10.1039/d5ta07667f**.

Acknowledgements

We are grateful for the ASRT for their financial support towards this work.

Notes and references

1 M. Kitano, Y. Inoue, Y. Yamazaki, F. Hayashi, S. Kanbara, S. Matsuishi, T. Yokoyama, S.-W. Kim, M. Hara and H. Hosono, *Nat. Chem.*, 2012, **4**, 934–940.
2 M. A. Sutton, D. Simpson, P. E. Levy, R. I. Smith, S. Reis, M. Van Oijen and W. I. M. De Vries, *Glob. Change Biol.*, 2008, **14**, 2057–2063.
3 T. H. Jeon, Z.-Y. Wu, F.-Y. Chen, W. Choi, P. J. J. Alvarez and H. Wang, *J. Phys. Chem. C*, 2022, **126**, 6982–6989.
4 G. Soloveichik, *Nat. Catal.*, 2019, **2**, 377–380.
5 J. Zheng, H. Zhou, C.-G. Wang, E. Ye, J. W. Xu, X. J. Loh and Z. Li, *Energy Storage Mater.*, 2021, **35**, 695–722.
6 M. M. Shi, D. Bao, B. R. Wulan, Y. H. Li, Y. F. Zhang, J. M. Yan and Q. Jiang, *Adv. Mater.*, 2017, **29**, 1606550.
7 Y. Wang, H. Li, W. Zhou, X. Zhang, B. Zhang and Y. Yu, *Angew. Chem.*, 2022, **134**, e202202604.
8 Y. Pan, H. Xu, H. Zhu, C.-J. Huang, Z. Zhi-Jie and G.-R. Li, *J. Mater. Chem. A*, 2025, **13**, 21181–21232.
9 Y. Wang, X. Lin, G. Zhang, H. Gao, Z.-J. Zhao, P. Zhang, T. Wang and J. Gong, *Proc. Natl. Acad. Sci. U. S. A.*, 2023, **120**, e2305604120.
10 W. Qiu, Y. Liu, M. Xie, Z. Jin, P. Li and G. Yu, *EES Catal.*, 2024, **2**, 202–219.
11 X. Gao, C. Zhu, C. Yang, G. Shi, Q. Xu and L. Zhang, *ACS Catal.*, 2024, **14**, 17871–17878.
12 S. M. Varghese, A. V. Gopinathan, S. Rathnakumaran, S. Sasikumar, S. Kunnikuruvan and R. R. Gangavarapu, *ACS Catal.*, 2025, **15**, 5982–5992.
13 Y. Zhao, Z. Bao, X. Bai, P. Xu, X. Shi, Q. Wu, Y. Jia, H. Zheng and L. Zheng, *Appl. Catal., B*, 2024, **357**, 124294.
14 H. Gao, G. Wang, Y. Fan, J. Wu, M. Yao, X. Zhu, X. Guo, B. Long and J. Zhao, *Sci. Rep.*, 2024, **14**, 16873.
15 X. Liu, A. H. W. Beusen, H. J. M. van Grinsven, J. Wang, W. J. van Hoek, X. Ran, J. M. Mogollón and A. F. Bouwman, *Nat Sustainability*, 2024, **7**, 891–900.
16 X. Zhang, E. A. Davidson, D. L. Mauzerall, T. D. Searchinger, P. Dumas and Y. Shen, *Nature*, 2015, **528**, 51–59.
17 X. Chen, M. Strokal, M. T. H. van Vliet, L. Liu, Z. Bai, L. Ma and C. Kroeze, *Environ. Sci. Technol.*, 2024, **58**, 9689–9700.
18 S. Zhang, J. Wu, M. Zheng, X. Jin, Z. Shen, Z. Li, Y. Wang, Q. Wang, X. Wang and H. Wei, *Nat. Commun.*, 2023, **14**, 3634.
19 Y. Wang, S. Wang, Y. Fu, J. Sang, P. Wei, R. Li, D. Gao, G. Wang and X. Bao, *Nat. Commun.*, 2025, **16**, 897.
20 P. Li, R. Li, Y. Liu, M. Xie, Z. Jin and G. Yu, *J. Am. Chem. Soc.*, 2023, **145**, 6471–6479.
21 Q. Hong, B. Miao, T. Wang, F. Li and Y. Chen, *Energy Lab*, 2023, **1**, 220022.
22 J. Li, G. Zhan, J. Yang, F. Quan, C. Mao, Y. Liu, B. Wang, F. Lei, L. Li and A. W. M. Chan, *J. Am. Chem. Soc.*, 2020, **142**, 7036–7046.
23 K. Fan, W. Xie, J. Li, Y. Sun, P. Xu, Y. Tang, Z. Li and M. Shao, *Nat. Commun.*, 2022, **13**, 7958.
24 F.-Y. Chen, Z.-Y. Wu, S. Gupta, D. J. Rivera, S. V. Lambeets, S. Pecaut, J. Y. T. Kim, P. Zhu, Y. Z. Finfrock and D. M. Meira, *Nat. Nanotechnol.*, 2022, **17**, 759–767.
25 W. He, J. Zhang, S. Dieckhöfer, S. Varhade, A. C. Brix, A. Lielpetere, S. Seisel, J. R. C. Junqueira and W. Schuhmann, *Nat. Commun.*, 2022, **13**, 1129.
26 M. Wei, S. Li, X. Wang, G. Zuo, H. Wang, X. Meng and J. Wang, *Adv. Energy Sustain. Res.*, 2024, **5**, 2300173.
27 M. Karamad, T. J. Goncalves, S. Jimenez-Villegas, I. D. Gates and S. Siahrostami, *Faraday Discuss.*, 2023, **243**, 502–519.
28 K. Zhang, Y. Liu, Z. Pan, Q. Xia, X. Huo, O. C. Esan, X. Zhang and L. An, *EES Catal.*, 2024, **2**, 727–752.
29 L. Bai, F. Franco, J. Timoshenko, C. Rettenmaier, F. Scholten, H. S. Jeon, A. Yoon, M. Rüscher, A. Herzog and F. T. Haase, *J. Am. Chem. Soc.*, 2024, **146**, 9665–9678.
30 A. M. Abdelmohsen, A. M. Agour, I. M. Badawy, G. E. Khedr, Y. Mesbah and N. K. Allam, *Sustain. Energy Fuels*, 2024, **8**, 3925–3932.
31 M. Zabilskiy, V. L. Sushkevich, D. Palagin, M. A. Newton, F. Krumeich and J. A. van Bokhoven, *Nat. Commun.*, 2020, **11**, 2409.
32 J. Lan, Z. Wang, C.-w. Kao, Y.-R. Lu, F. Xie and Y. Tan, *Nat. Commun.*, 2024, **15**, 10173.
33 J. J. Wang, H. T. D. Bui, X. Wang, Z. Lv, H. Hu, S. Kong, Z. Wang, L. Liu, W. Chen and H. Bi, *J. Am. Chem. Soc.*, 2025, **147**, 8012–8023.
34 J. Nakamura, T. Fujitani, S. Kuld, S. Helveg, I. Chorkendorff and J. Sehested, *Science*, 2017, **357**, eaan8074.
35 N. Bahnasawy, A. M. Elbanna, M. Ramadan and N. K. Allam, *Sci. Rep.*, 2022, **12**, 16785.
36 S. Dongare, N. Singh, H. Bhunia and P. K. Bajpai, *Electrochim. Acta*, 2021, **392**, 138988.
37 I. M. Badawy, A. M. Ismail, G. E. Khedr, M. M. Taha and N. K. Allam, *Sci. Rep.*, 2022, **12**, 13456.
38 R. Leil, M. M. Abodouh, N. Javed, S. Sreekumar, H. Pacheco, N. Tarek, D. M. O'Carroll and N. K. Allam, *Energy Adv.*, 2024, **3**, 430–441.
39 O. I. Zaytsev, M. A. Belokozenko, G. P. Lakienko, E. E. Levin, V. A. Nikitina and S. Y. Istomin, *J. Electroanal. Chem.*, 2024, **975**, 118795.
40 S. Dongare, N. Singh and H. Bhunia, *Appl. Surf. Sci.*, 2021, **556**, 149790.
41 A. Adalder, S. Paul, N. Barman, A. Bera, S. Sarkar, N. Mukherjee, R. Thapa and U. K. Ghorai, *ACS Catal.*, 2023, **13**, 13516–13527.
42 S. Paul, S. Sarkar, A. Adalder, S. Kapse, R. Thapa and U. K. Ghorai, *ACS Sustain. Chem. Eng.*, 2023, **11**, 6191–6200.
43 S. Bhowmick, A. Adalder, A. Maiti, S. Kapse, R. Thapa, S. Mondal and U. K. Ghorai, *Chem. Sci.*, 2025, **16**, 4806–4814.
44 S. Sarkar, A. Adalder, S. Paul, S. Kapse, R. Thapa and U. K. Ghorai, *Appl. Catal., B*, 2024, **343**, 123580.
45 C. Wang, F. Ye, J. Shen, K.-H. Xue, Y. Zhu and C. Li, *ACS Appl. Mater. Interfaces*, 2022, **14**, 6680–6688.
46 M. Teng, J. Ye, C. Wan, G. He and H. Chen, *Ind. Eng. Chem. Res.*, 2022, **61**, 14731–14746.

47 R. Yang, H. Li, J. Long, H. Jing, X. Fu and J. Xiao, *ACS Sustain. Chem. Eng.*, 2022, **10**, 14343–14350.
48 N. Zhou, Z. Wang, N. Zhang, D. Bao, H. Zhong and X. Zhang, *ACS Catal.*, 2023, **13**, 7529–7537.
49 S. Ye, X. Yang, Z. Huang, Z. Chen, W. Chen, T. Huang, Z. Ou, W. Xiong, Y. Li and X. Ren, *Sci. China Mater.*, 2023, **66**, 3573–3581.
50 S. Liang, X. Teng, H. Xu, L. Chen and J. Shi, *Angew. Chem.*, 2024, **136**, e202400206.
51 S. Manohar, J. Ananthaswamy and G. Atkinson, *J. Chem. Soc., Faraday Trans.*, 1992, **88**, 991–995.
52 M. Mizuhata, *Electrochemistry*, 2022, **90**, 102011.
53 T. Jiang, Y. Wang, D. Meng and D. Wang, *J. Mater. Sci.: Mater. Electron.*, 2016, **27**, 12884–12890.
54 E. Sidot, A. Kahn-Harari, E. Cesari and L. Robbiola, *Mater. Sci. Eng. A*, 2005, **393**, 147–156.
55 A. Paliwal, C. D. Bandas, E. S. Thornburg, R. T. Haasch and A. A. Gewirth, *ACS Catal.*, 2023, **13**, 6754–6762.
56 W. Yu, J. Yu, M. Huang, Y. Wang, Y. Wang, J. Li, H. Liu and W. Zhou, *Energy Environ. Sci.*, 2023, **16**, 2991–3001.
57 Z. Li, R. M. Yadav, L. Sun, T. Zhang, J. Zhang, P. M. Ajayan and J. Wu, *Appl. Catal., A*, 2020, **606**, 117829.
58 H. Idriss, *Surf. Sci.*, 2021, **712**, 121894.
59 M. C. Biesinger, *Surf. Interface Anal.*, 2017, **49**, 1325–1334.
60 T. Baran, A. Visibile, M. Busch, X. He, S. Wojtyla, S. Rondinini, A. Minguzzi and A. Vertova, *Molecules*, 2021, **26**, 7271.
61 V. Srivastava and A. K. Choubey, *Mater. Res. Express*, 2020, **6**, 1250i1257.
62 R. Yuan, X.-H. Wang, S.-B. Yin, X. Ai, Y.-C. Yin, Y. Chen and S.-N. Li, *ACS Mater. Lett.*, 2025, **7**, 2310–2318.
63 M. Ricci, W. Trewby, C. Cafolla and K. Voïtchovsky, *Sci. Rep.*, 2017, **7**, 43234.
64 Z. Wang, C. Sun, X. Bai, Z. Wang, X. Yu, X. Tong, Z. Wang, H. Zhang, H. Pang and L. Zhou, *ACS Appl. Mater. Interfaces*, 2022, **14**, 30969–30978.
65 Y. Zhao, R. Shi, X. Bian, C. Zhou, Y. Zhao, S. Zhang, F. Wu, G. I. N. Waterhouse, L. Z. Wu and C. H. Tung, *Adv. Sci.*, 2019, **6**, 1802109.
66 A. A. Akar, R. Seif, M. M. Taha, A. A. M. Ismail and N. K. Allam, *Mater. Today Sustain.*, 2023, **24**, 100477.
67 A. A. Akar, E. Yousry, R. Seif and N. K. Allam, *Fuel*, 2025, **386**, 134266.
68 A. Feng, Y. Hu, X. Yang, H. Lin, Q. Wang, J. Xu, A. Liu, G. Wu and Q. Li, *ACS Catal.*, 2024, **14**, 5911–5923.
69 H. G. El-Aqapa, G. E. Khedr, I. M. Badawy, A. M. Agour, A. M. Abdelmohsen and N. K. Allam, *J. Mater. Chem. A*, 2025, **13**, 7091–7095.
70 L. Yu and R. Akolkar, *J. Electrochem. Soc.*, 2016, **163**, D247.
71 B. Hazelgrove, L. Matter, B. Raos, B. Harland, L. Cheng, M. Asplund and D. Svirskis, *Nat. Rev. Electr. Eng.*, 2025, 1–15.
72 B. Hirschorn, M. E. Orazem, B. Tribollet, V. Vivier, I. Frateur and M. Musiani, *Electrochim. Acta*, 2010, **55**, 6218–6227.
73 P. Córdoba-Torres, T. J. Mesquita and R. P. Nogueira, *J. Phys. Chem. C*, 2015, **119**, 4136–4147.
74 M. Paunovic, M. Schlesinger and D. D. Snyder, *Modern Electroplating*, 2010, pp. 1–32.
75 C. Lei, F. Markoulidis, Z. Ashitaka and C. Lekakou, *Electrochim. Acta*, 2013, **92**, 183–187.
76 T. H. Wan, M. Saccoccio, C. Chen and F. Ciucci, *Electrochim. Acta*, 2015, **184**, 483–499.
77 C. Plank, T. Rüther, L. Jahn, M. Schamel, J. P. Schmidt, F. Ciucci and M. A. Danzer, *J. Power Sources*, 2024, **594**, 233845.
78 A. Rampf, C. Marchfelder and R. Zeis, *Electrochim. Acta*, 2025, **514**, 145583.
79 B. A. Boukamp, *J. Phys.: Energy*, 2020, **2**, 042001.
80 Z. Huang, L. Shang, H. Qi, Z. Zhao, B. Tu, W. Yang and M. Cheng, *ChemElectroChem*, 2019, **6**, 1668–1672.
81 J. Zhao, J. Xu and L. Shi, *New J. Chem.*, 2024, **48**, 13233–13237.
82 Y.-Y. Lou, Q.-Z. Zheng, S.-Y. Zhou, J.-Y. Fang, O. Akdim, X.-Y. Ding, R. Oh, G.-S. Park, X. Huang and S.-G. Sun, *ACS Catal.*, 2024, **14**, 5098–5108.
83 E. Murphy, Y. Liu, I. Matanovic, M. Rüscher, Y. Huang, A. Ly, S. Guo, W. Zang, X. Yan and A. Martini, *Nat. Commun.*, 2023, **14**, 4554.
84 Y. Wang, A. Xu, Z. Wang, L. Huang, J. Li, F. Li, J. Wicks, M. Luo, D.-H. Nam and C.-S. Tan, *J. Am. Chem. Soc.*, 2020, **142**, 5702–5708.
85 Y. Zhu, H. Duan, C. G. Gruber, W. Qu, H. Zhang, Z. Wang, J. Zhong, X. Zhang, L. Han and D. Cheng, *Angew. Chem., Int. Ed.*, 2025, e202421821.
86 Y. Lu, F. Yue, T. Liu, Y.-C. Huang, F. Fu, Y. Jing, H. Yang and C. Yang, *Nat. Commun.*, 2025, **16**, 2392.
87 A. Garg, A. Saha, S. Dutta, S. K. Pati, M. Eswaramoorthy and C. N. R. Rao, *ACS Appl. Mater. Interfaces*, 2024, **16**, 36392–36400.
88 H. Yin, Z. Chen, S. Xiong, J. Chen, C. Wang, R. Wang, Y. Kuwahara, J. Luo, H. Yamashita and Y. Peng, *Chem Catal.*, 2021, **1**, 1088–1103.
89 Y. Zhang, S. Li, W. Zheng and X. Wang, *Nano Res. Energy*, 2023, **2**, e9120068.